Empirical correlation of quantified hard carbon structural parameters with electrochemical properties for sodium-ion batteries using a combined WAXS and SANS analysis

Laura Kalder [a], Annabel Olgo [a], Jonas Lührs [b], Tavo Romann [a], Riinu Härmas [a], Jaan Aruväli [c], Pouya Partovi-Azar [b], Albrecht Petzold [d], Enn Lust [a], Eneli Härk [e,*]

[a] *Institute of Chemistry, University of Tartu, Ravila 14a, 50411, Tartu, Estonia*
[b] *Institute of Chemistry, Martin Luther University Halle-Wittenberg, Von-Danckelmann-Platz 4, 06120 Halle (Saale), Germany*
[c] *Institute of Ecology and Earth Sciences, University of Tartu, Ravila 14a, 50411, Tartu, Estonia*
[d] *Institute of Physics, Faculty of Natural Sciences II, Martin-Luther-Universität Halle-Wittenberg, Von-Danckelmann-Platz 3, 06120 Halle (Saale), Germany*
[e] *Helmholtz-Zentrum Berlin für Materialien und Energie, Hahn-Meitner-Platz 1, 14109, Berlin, Germany*

ABSTRACT

This study highlights the advantages of using wide-angle X-ray scattering (WAXS) and small-angle neutron scattering (SANS) methods to analyse turbostratic d-glucose-derived hard carbons (GDCs) over a wide range of length scales. It demonstrates the reasons for the superior performance of hard carbons (HCs) pyrolysed at 1100 °C compared to those pyrolysed at 700 °C, 1000 °C, or 1400 °C in sodium-ion batteries (SIBs). Twelve WAXS and thirteen SANS structural parameters were simultaneously determined for HCs. The investigation incorporates WAXS-derived interlayer spacing, a_3, into the SANS analysis of HCs. The Ruland and Smarsly algorithm is emphasised over the commonly used Scherrer and Bragg equations. Thus, the collective analysis of nanostructure highlights the necessity for a revision in applying widely used characterisation techniques when dealing with disordered HCs. The study suggests that an a_3 value of 0.373 nm best suits GDC-1100 as a SIB anode material. Comparing HCs prepared at different pyrolysis temperatures, GDC-1100 exhibits the most compatible parameters, resulting in the highest specific capacity value. The model-free SAS analysis indicates hierarchical structural changes at nanoscopic (SANS) and atomic (WAXS) scales simultaneously. The interplay between dynamic a_3 and static parameters, such as the graphene layer extent L_a and the Ruland length, l_R, favours plateau capacity, contributing to sodium ion storage. The study demonstrates the suitability of the WAXS/SANS toolbox for empirically correlating hard carbons' structural characteristics with the electrochemical performance of SIBs.

1. Introduction

Beyond lithium-ion batteries, sodium-ion batteries (SIBs) reach a sodium (Na) storage capacity of up to 420 mAh g^{-1} [1–9], but the exact mechanism of the storage of sodium ions in a hard carbon (HC) anode is still a scientific challenge [4,6,7,10–12]. In numerous reports, the characteristics of HC responsible for the storage of Na ions are porosity (pore filling theory), stacking (intercalation), and the lateral extent of the graphene sheets (adsorption) [1,3,9,13–18]. Hard carbon structure is commonly described with *ex situ* methods such as Raman spectroscopy [19–23], gas adsorption [10,13,20,24], high-resolution transmission electron microscopy (HRTEM) [13,14,22,24], X-ray diffraction (XRD)

[19,21,24] methods. Raman spectroscopy is a relatively simple and non-destructive method for describing the electronic structure of carbon material. Indirectly, the average graphene layer extent has also been estimated based on the Raman spectra using empirical equations [1,3,6, 9,15,24]. However, interpreting Raman spectra is complex and requires careful modelling [25–27,23]. The gas adsorption method is a standardised way to get information about the open porous structure of the carbon material, e.g. the pore volume and pore size distribution and the specific surface area [28,29]. Yet, for the detailed interpretation of gas adsorption data, models with specific assumptions on the pore shape or surface are applied, which can also lead to inaccurate results, for instance, a substantial underestimation of the pore accessibility [28,

30–32]. HRTEM can be used to determine the interlayer distances qualitatively in small sample regions [14,21,24,30,33], thus offering a precise and straightforward description of a very small part of the local carbon structure [34]. Meanwhile, XRD[1] is a non-destructive bulk technique to determine the averaged structure at the atomic scale [7,10, 29]. For carbon materials, the Bragg equation is commonly used to determine interlayer distances based on the position of the (002) reflections in the XRD pattern, and the Scherrer equation [35–37] is often used to estimate the stacking size and, in some cases, the graphene layer extent based on the reflection widths. Considering the suitability of the XRD technique for both crystalline and non-crystalline materials, it is more fitting to utilize wide-angle X-ray scattering (WAXS) for non-graphitic carbon materials. This is due to the constrained length scale range commonly encountered in traditional laboratory XRD setups, which diminishes the quantity of obtainable reflections [38]. All the more reason that the turbostratic structure in carbon materials (as illustrated in Supplementary Information (SI), Fig. S1a) are primarily explored and associated with the electrochemical sloping and plateau capacities in articles pertaining to sodium-ion batteries (SIBs) [3,6,7,9, 10,12,13,15,20,21,24,37,39–43] with the following *ex situ* features:

- average interlayer spacing, a_3,
- average layer stacking size, L_c,
- the average number of layers in a stack, N, and
- the average graphene layer extent, L_a.

Nonetheless, numerous necessary inquiries persist concerning the consequences of applying the Scherrer and Bragg equations to disordered carbon materials. Firstly, the hard carbons diffraction curve peaks exhibit significant broadening and asymmetry (Fig. S1b in SI). Hence, accurately determining the position of the (002) peak maxima, which defines the spacings between graphene layers, poses a challenge. Secondly, for the disordered materials, the peak broadening is caused by the defects and the curvature of the graphene sheets, different orientations of the stacks, and the stacking size. Thirdly, the Scherrer equation presupposes that the broadening of the peak is solely attributed to the crystallite size, disregarding the potential impact of various forms of disorder, such as defects and curvature, on the peak's width. Therefore, using the estimated interlayer spacing, layer stacking size or the number of layers in a stack derived from the Scherrer and Bragg approaches for disordered carbons needs amendment. As opposed to the typical XRD pattern analysis approach, the algorithm derived by Ruland and Smarsly [44] for disorganised sp^2 carbon materials uses data from the entire pattern, not only from specific peaks. This algorithm enables the reliable quantitative evaluation of parameters (e.g. a_3, L_c, N, L_a) [44–48].

Small angle scattering methods, i.e. neutron / X-ray scattering (SANS / SAXS), provide averaged information on the nanoscopic scale's carbon materials structure and porosity (from 0.8 to 100 nm). The data analysis can be carried out with the help of different models or also through model-free approaches [7,9,40,49–53]. For example, in a study conducted by Simone et al. in 2016, SAXS was employed to examine the porous architecture of cellulose-derived carbons utilised as anode materials for SIBs [9]. In that context, and the investigation presented by Palm et al. in 2021 [53], the Guinier-Porod model was applied to analyse and interpret small-angle scattering data of carbon powders. Moreover, the model-free data analysis, utilising a combination of Schiller, Mering,

Perret, and Ruland approximations [54–57], facilitates the assessment of the porous structure, encompassing the determination of open and closed porosity values [30]. Utilising this approach, it is also possible to obtain the particle size distribution with a diameter from 0.1 to 1 nm; in some cases, information on the shape of the particles is also available [54,58–60]. While research has acknowledged the significance of open and closed porosity in the anode material's capacity to store sodium ions, there has been a shortage of comprehensive examinations of the porous structure in SIB-related literature, including comparing parameters like pore wall thickness, pore curvature, or the degree of disorder [6,18,30]. Therefore, it is favoured to adopt scattering (wide angle and small angle scattering [46,54,58,61]) methods to receive information complementary to gas adsorption [3,6,10,13,14,20,21,24,28,29,32,60] and HRTEM about the average properties of the bulk material.

Although interpreting scattering data requires careful and complicated data analysis [47,54], the precise estimation of HC nanostructure parameters could aid in developing a better and uniform understanding of the sodium storage mechanisms in HCs. Previous research [12,39,42, 62], which used hard carbons synthesised under identical conditions, has primarily concentrated on electrochemical assessments to pinpoint the most optimal HC for SIBs. In this work, our primary objective is not to improve electrochemical performance in these hard carbon-based half-cells but rather to delve into observations such as the potential composition profile, i.e., capacity changes characterised by both sloping and plateau behaviour based on structural properties during the first cycle that may indicate nanostructural variations that underlie favourable electrochemical measurements and material suitability. We highlight the limitations of *ex situ* characterisation analysis via Scherrer and Bragg equations and improve fundamental understanding over a wide range of length scales (0.1–70 nm) for disorganised HCs. Herein, we focus on combined approximations of Schiller, Mering, Perret, and Ruland [54–57] for analysis of SANS data, Ruland and Smarsly [44] approach for analysis of WAXS data to give a precise and quantitative description of the HCs that have been derived from d-glucose via hydrothermal carbonisation at different fixed pyrolysis temperatures [12, 39,42,62]. The study addresses why an HC originating from the same source, carbonised at various fixed temperatures, appears to exhibit superior performance in SIBs compared to another member of this "family."

2. Experimental

2.1. Hydrothermally derived hard carbons from d-glucose

Four hard carbons (Table 1) were produced from d-glucose [37,40] through a combination of hydrothermal carbonisation, pyrolysis, and the post-treatment (except for GDC-1400) method described in reference [39]. These different hard carbons are denoted as GDC-X, where GDC stands for glucose-derived carbon, and X stands for the pyrolysis temperature (T_p). Shortly, 2 M aqueous d-glucose solution hydrothermal carbonation was performed at 200 °C for 24 h [62]. Subsequently, the carbonaceous product underwent pyrolysis (in atmosphere of argon) at the specified temperatures given in Table 1, followed by post-treatment with H_2 to eliminate surface functional groups, except for GDC-1400

Table 1
The synthesis conditions of analysed carbon materials [12,39,42,62].

Hard carbon[a]	T_p[b], gas, time	Post-treatment
GDC-700	**700 °C**, Ar, 2 h	800 °C, H_2, 2 h
GDC-1000	**1000 °C**, Ar, 2 h	800 °C, H_2, 2 h
GDC-1100	**1100 °C**, Ar, 2 h	800 °C, H_2, 2 h
GDC-1400	**1400 °C**, Ar, 2 h	–

[a] GDC-X, where X denotes pyrolysis temperature, GDC stands for glucose-derived carbon, and [b]T_p indicates pyrolysis temperature. Pyrolysis have been carried out in atmosphere of argon.

---

[1] In the literature this method is often named X-ray Diffraction (XRD). However, the term 'XRD' refers to having crystalline materials as samples resulting with sharp reflections in the corresponding XRD patterns. Wide angle X-ray scattering (WAXS) is a similar method to XRD in terms of the measured scattering vector, q, range (approx. 3–60 nm^{-1}) using the Bragg-Brentano geometry. However, since the term *scattering* is more suitable than the term *diffraction* in the case of non-crystalline materials, the term WAXS is used to refer to this method in this work.

[39].

In this study, we subjected GDC-X to H_2 reduction treatment. Nevertheless, numerous studies have demonstrated that hard carbon, derived from different precursors, might not necessitate H_2 reduction treatment for the removal of a significant portion of functional groups, such as carboxyl groups. This omission enhances the performance of sodium ion storage [63,64].

2.2. Electrochemical characterisation of sodium-ion batteries based on GDC-X

The electrochemical characterisation of the half-cells was conducted within CR2032-type coin cells, which were assembled in an Argon-filled glove box (MBRAUN, <1 ppm of O_2 and <1 ppm of H_2O). In these cells, the working electrode was composed of a tape-casted hard carbon (GDC-X) electrode [42,43] with the preparation details provided in Chapter 2 of the SI. The counter electrode was a sodium metal disk (Acros, 99.8 %). These two electrodes were separated by a glass fiber separator (1.55 mm, EL-Cell GmbH). The glass fiber separator was pre-wetted with 1 M $NaPF_6$ dissolved in a mixture of ethylene carbonate (EC, Sigma-Aldrich, 99 %) and propylene carbonate (PC, Sigma-Aldrich, 99.7 %) with a volume ratio of 1:1.

The galvanostatic charging/discharging (GCD) method was used to evaluate the electrochemical performance of the GDC-X half-cells. Half-cell galvanostatic cycling experiments were performed using PMC–1000 potentiostat (Princeton Applied Research, Oak Ridge, TN, USA) within the potential range of $E = 0.005$–1.5 V vs Na^+/Na at a specific current of 25 mA g^{-1} for three cycles.

2.3. Wide-angle X-ray scattering

The materials' wide-angle X-ray scattering measurements were performed on a Bruker D8 Advance (Bruker Corporation) diffractometer using Cu Kα radiation ($\lambda = 1.5406$ Å). The measurement was performed in Bragg-Brentano geometry and 1D detector, with a step $d\theta = 0.02°$ and a total counting time of 576 s per step in the region $3 < 2\theta < 93°$ was used. The samples were pressed into a 0.5 mm deep silicon monocrystal sample holder. The parameters related to the structure were calculated based on the modelled curve via the Ruland and Smarsly algorithm, described in SI chapter 1.1. The Ruland and Smarsly approach permits the determination of up to 18 structural parameters (12 of them mathematically independent) of the disorganised carbon materials [42,43].

2.4. Small angle neutron scattering

SANS measurements were performed on a small angle scattering instrument V4 at the cold neutron source of the Helmholtz-Zentrum Berlin research reactor [65]. The neutron flux measured on the V4 instrument was $\sim 10^6$ cm^{-2} s^{-1} for the two wavelengths used, $\lambda = 4.5$ Å and 6.07 Å [65]. A detailed model-free analysis of the SANS scattering curves was performed using a combination of Schiller, Mering, Perret, and Ruland approximations [54–57] (see SI chapter 1.2). This model-free approach allows for the determination of up to 13 structurally significant parameters that are both mathematically independent and physically meaningful.

2.5. Density-functional theory

Atomistic calculations are conducted employing density-functional theory (DFT). Graphene sheets featuring armchair and zigzag edges are modelled, with structures incorporating five carbon rings along their width in each scenario. Both fully hydrogenated and hydrogen-free edges are considered. Atomic positions are iteratively optimised until the maximum atomic force component reaches 0.02 eV/Å. All DFT calculations are performed using the CP2K software [66]. A double zeta plus polarisation basis function optimised for molecular systems

(DZVP-MOLOPT) [67] along with Geodecker-Teter-Hutter (GTH) pseudopotentials are used [68]. The approximations of exchange and correlation effects are made through the utilisation of the Becke-Lee-Yang-Parr (BLYP) functional [69,70] together with the DFT-D3 method [71], which accounts for long-range dispersion interactions. The interaction energies between the Na cation and the graphene edges are calculated using the counterpoise correction [72] to account for the basis set superposition error.

3. Results and discussion

3.1. Evaluating sloping and plateau capacity of SIB anode half cells

The cycling performance of the GDC-X electrode material was assessed using a galvanostatic charging and discharging method at a current density of 25 mA g^{-1}. The analysis was conducted on the sodiation curve of the second cycle after complete electrochemical wetting had been accomplished during the first cycle. The first three cycles of the sodiation-desodiation curves for various anode-active materials are presented in Fig. S2 in SI. The discharge curve of the 2nd cycle was divided into regions – the sloping region (marked as a red line in Fig. 1a) and the plateau region (marked as blue line in Fig. 1a) [73,74]. The half-cells containing GDC-X demonstrate a spectrum of specific capacities, ranging from 196.8 to 321.3 mAh g^{-1}, as also previously by R. Väli et al. [42,43]. The highest calculated specific capacity value for the second discharge cycle (as shown in Fig. 1b) slightly exceeded 320 mAh g^{-1} for anodes based on the GDC-1100 anode in SIB half-cells. The galvanostatic charging/discharging data for the SIB anode half-cells reveal a noticeable shift in the electrochemical performance when comparing GDC-1000 and GDC-1100 anodes (Fig. 1 and Fig. S2 in SI).

As reported in previous studies, half-cells featuring HC anode materials pyrolysed at elevated temperatures (T_p) displayed a pronounced plateau capacity, indicative of enhanced sodium ion storage within closed pores [3,7,9,75]. On the other hand, the sloping region has been associated with sodium ion adsorption on defect sites of the HC anodes [7,41]. Fig. 1b shows that the specific capacities of SIB half-cells containing hard carbons synthesised at 700 °C and 1000 °C exhibit a prevalence of sloping capacity, whereas those produced at 1100 °C and 1400 °C predominantly showcase plateau capacities. In addition, we can observe that an increase in pyrolysis temperature does not change the slope-to-plateau capacity ratio but only decreases the specific capacity value. It is essential to highlight that the H_2 post-treatment employed in synthesizing GDC-1100, when compared to GDC-1400, has led us to the conclusion that the electrochemical performance of GDC-X at these elevated temperatures is seemingly unaffected by the presence or absence of additional functional groups remaining in the material structure [63]. This raises the question of which specific structural parameter causes the change between 1000 °C and 1100 °C that seems to support the ratio change of the sloping and plateau capacity.

Initially, an effort was undertaken to clarify alterations in the porous nanostructure of GDC-X materials through gas adsorption measurements involving CO_2 and N_2. The adsorption data were fitted using non-local density functional theory, and the heterogeneous pore surface model was used to calculate the pore size distribution. The differential pore size distributions vs pore widths for hard carbons pyrolysed at either 1000 °C or 1100 °C exhibit overlapping data, as illustrated in Fig. S3a in SI. We can conclude that both HC samples have nearly identical open porosity and comparable average pore size. As a result, it is challenging to identify significant distinctions in the nanostructure of these two materials based on the data.

Following this, the objective was to gain an understanding of the crystallographic and electronic structure of GDC-X, employing Raman spectroscopy as a surface-sensitive technique (described in SI chapter 6, Fig. S4) [23,76]. Five distribution functions were used to deconvolution the first-order region (Figs. S4d-f) [77]. Figures S4a-c in SI illustrate
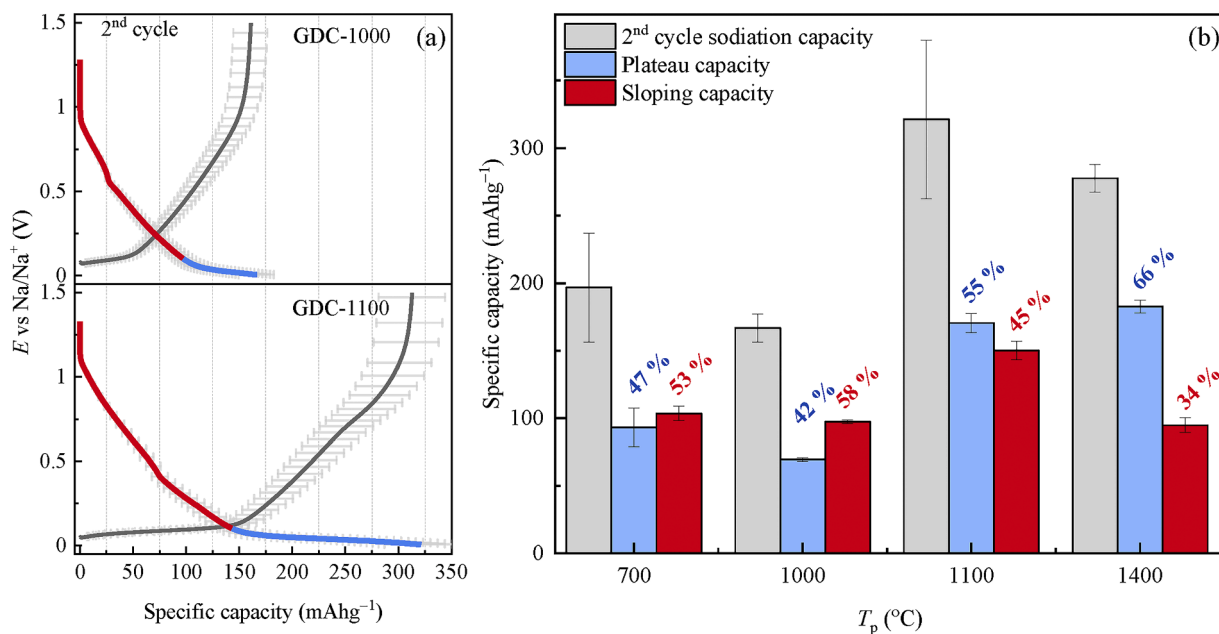
Fig. 1. (a) Sodiation-desodiation of electrochemical half-cells during the second cycle, featuring GDC-1000 (above) and GDC-1100 (below) HC anodes (Data normalisation is given in Table S2 in SI). The sodiation curves are divided into two regions: the sloping region (red line, $E > 0.1$ V) and the plateau region (blue line, $E < 0.1$ V). (b) The ratio of second-cycle sloping and plateau capacities in electrochemical half-cells constructed with hard carbon anodes synthesised at various pyrolysis temperatures.

broad, well-known d- and G-bands and, additionally, alteration in the intensity and shape of the 2D band in GDC-1400 compared to GDC-1000 and GDC-1100. While the Raman shift of the d-band remains unchanged, the G-band shows a non-systematic shift with increasing pyrolysis temperature between 1000 °C and 1400 °C (Fig. S4b in SI). In the GDC-1400 spectrum, the G-band displays a blue-shift compared to the spectra of GDC-1000 and GDC-1100, signifying a reduction in the strength of the in-plane C–C bond and an expansion of the C–C distance. The spectral parameters listed in Table S3 showed that the d-band's full width at half maximum (FWHM) and $\frac{A\sum_D}{A\sum_G}$ ratio values do not exhibit a distinct trend while elevating the pyrolysis temperature. The FWHM attains its maximum value at approximately 157 ± 2 cm^{-1} for a carbon material pyrolysed at 1100 °C (see Table S3 in SI). Simultaneously, the $\frac{A\sum_D}{A\sum_G}$ ratio values coincide for GDC-1000 and GDC-1100 materials [78]. Our results demonstrate that although the *ex situ* Raman analysis unequivocally aligns with the data derived from gas adsorption measurements, it proved insufficient in elucidating the electrochemical measurement results.

Subsequently, a combination of WAXS (at length scales ranging from 0.1 to 2 nm) and SANS (from 0.6 to 70 nm) methods was employed to comprehensively describe the layered and porous nanostructures of GDC-X HCs, encompassing assessments of open and closed porosity. A comprehensive examination of these length scales will enable us to establish an empirical correlation between specific slope capacity and plateau capacity values and structural parameters, providing insights into crucial SIBs-related parameters.

3.2. WAXS layered structural parameters of the disorganised carbon materials

The WAXS patterns for d-glucose-derived carbons indicate that all the studied materials have highly turbostratic layered structures due to the characteristic reflexes of non-graphitic carbons (002), (10), and (11) (Fig. 2 and Fig. S5 in SI). The scattering curve of GDC-700 contains slightly more diffuse peaks than those seen in the GDC-1400, indicating

a slight ordering of the carbon material with a remarkable increase in the T_p. The measured and fitted (Ruland and Smarsly algorithm [44]) scattering curves are presented in Fig. 2 alongside the corresponding deviation, and the obtained nanostructural parameters are tabulated in Table 2 (Eqs. S1 – S8 in SI).

The pyrolysis temperature, T_p, impacts the extent of the graphene layers' L_a and the chord length, l values (Eq. S3 in SI). Elevating the pyrolysis temperature leads to the formation of extended graphene layers compared to the results established at lower temperatures; for example, L_a for GDC-700 is 4.2 ± 0.7 nm, but for GDC-1400, L_a is 10 ± 2 nm. The chord length, l, is proportional to the graphene layer extent; therefore, the same relation with pyrolysis temperature appears. In addition, T_p also affects the stacking of the graphene layers, i.e., at the increased T_p, the average stack height L_c is higher (from 0.55 ± 0.02 nm to 0.83 ± 0.04 nm), as well as the number of layers per stack N (Eqs. S6 and S7 in SI). The polydispersity of stack height, κ_c (Eq. S8 in SI), is smaller in the materials with higher T_p. These parameter changes reflect the higher degree of order in the HC when pyrolysis has been carried out at higher temperatures. However, WAXS analysis demonstrated that T_p did not significantly influence the interlayer spacing a_3, the carbon-carbon bond length l_{cc}, the standard deviation of the first neighbour distribution σ_1, and the homogeneity of the layer stack, η, given in Table 2 (Eqs. S4 and S5 in SI).

These results are supported by previous studies analysing the structure of carbon materials [31,34,79–81], which suggest that the higher pyrolysis temperature results in a material with higher crystallinity and described with larger graphene layer extent, L_a, and average stack height, L_c. The temperature dependence of the L_a parameter is evident in the current and previous studies [22,23,47,82]. The values of the L_a parameter obtained for different carbon materials vary from 1 nm to 20 nm in the literature. Most commonly for HCs, the L_a values under 10 nm have been published for SIB anode materials. However, in SIB-related studies, the L_a parameter is often calculated based on the Raman D and G bands data [3,6,21,22,24]. For instance, Tonnoir et al. (2023) [83] conducted an in-depth analysis of Raman spectra in hard carbons, exploring *in situ* sodium intercalation between graphene layers. It is worth noting that, previous research has demonstrated notable
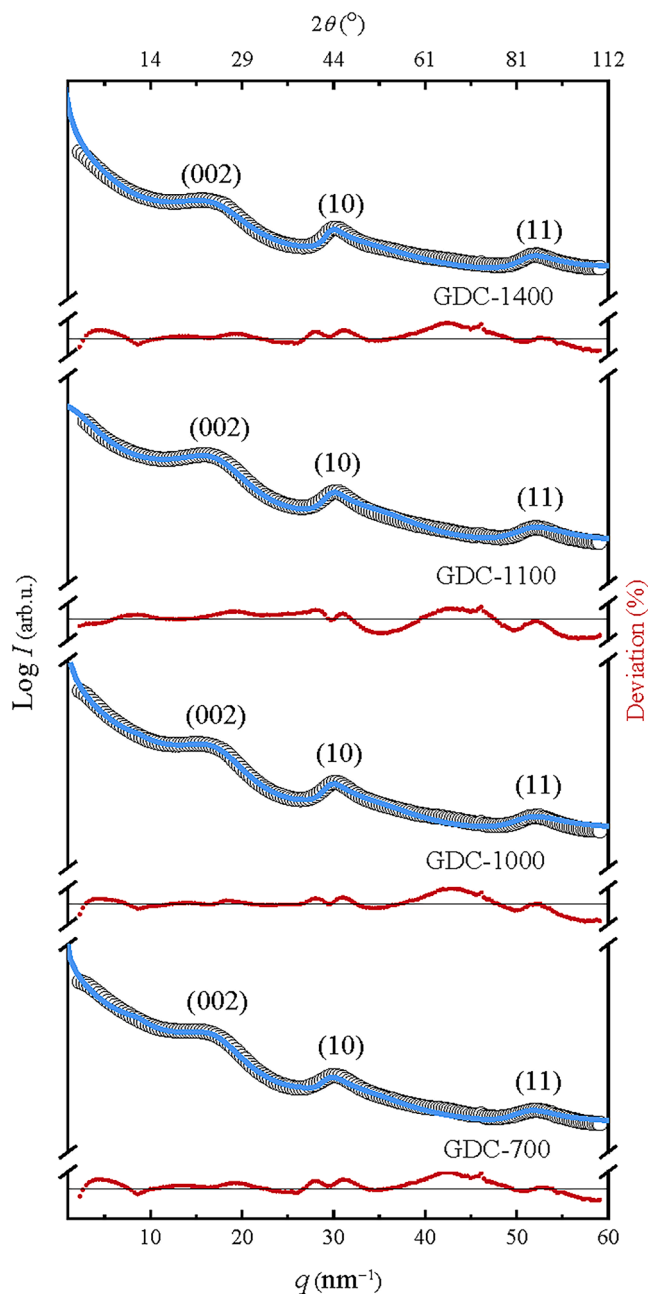
Fig. 2. WAXS scattering patterns (black), fitted curves (blue line) and deviations (red) of the investigated hard carbons GDC-1400, GDC-1100, GDC-1000, and GDC-700. The deviation between all materials' measured and fit curves ranges from −3 % to 3 %.

Table 2
Nanodomain structural parameters determined from WAXS analysis.

Parameter		GDC-700	GDC-1000	GDC-1100	GDC-1400	Trend
Layer structure	L_a (nm)	4.2 ± 0.7	6.3 ± 0.8	7 ± 1	10 ± 2	↑
	l (nm)	3.3 ± 0.6	5.0 ± 0.6	5.7 ± 0.8	8.0 ± 1.7	↑
	l_{CC} (nm)	0.142 ± 0.005	0.142 ± 0.005	0.141 ± 0.002	0.141 ± 0.005	–
	σ_1	0.166 ± 0.001	0.191 ± 0.005	0.191 ± 0.008	0.156 ± 0.005	–
Stacking of graphene layers Stacking of graphene layers	N	1.50 ± 0.06	1.8 ± 0.1	2.17 ± 0.07	2.3 ± 0.1	↑
	L_c (nm)	0.55 ± 0.02	0.64 ± 0.04	0.81 ± 0.03	0.83 ± 0.04	↑
	κ_c	3.2 ± 0.5	1.4 ± 0.1	0.48 ± 0.02	0.296 ± 0.002	↓
	a_3 (nm)	0.366 ± 0.003	0.365 ± 0.003	0.373 ± 0.002	0.365 ± 0.002	–
	$a_{3,min}$ (nm)	0.30 ± 0.03	0.30 ± 0.02	0.34 ± 0.02	0.31 ± 0.02	–
	σ_3 (nm)	0.040 ± 0.005	0.044 ± 0.003	0.060 ± 0.003	0.041 ± 0.001	–
	η	0.96 ± 0.01	0.95 ± 0.02	0.99 ± 0.01	0.84 ± 0.02	–
	e_o	0.258 ± 0.010	0.176 ± 0.005	0.110 ± 0.005	0.075 ± 0.007	↓

L_a – average graphene layer extent (↑); l – average chord length (↑); l_{CC} – carbon-carbon bond length; σ_1 – standard deviation of first-neighbour distribution; N – average layers per stack (↑); L_c – average stack height (↑); κ_c – polydispersity of stack height (↓); a_3 – average interlayer spacing; $a_{3,min}$ – minimum interlayer spacing; σ_3 – standard deviation of the distance between layers; η – homogeneity of stacks; e_o – parameter of preferred orientation (↓). The error values have been estimated by changing the parameters one by one until the deviation of the fit changed by 5 % [47]. WAXS parameters with fixed values are displayed in Table S1 with the SI fitting process description (chapter 1.1).

disparities between the L_a values derived from Raman spectra and those obtained from WAXS patterns [77]. In the present study, the graphene layer extent obtained for HC derived from glucose ranges from 4.2 ± 0.7 nm to 10 ± 2 nm, with an increase in pyrolysis temperature.

Nonetheless, interpreting these findings is not straightforward, given that one of the underlying assumptions of the Ruland and Smarsly algorithms is that the graphene layers are flat [44]. Based on HRTEM micrographs of disordered carbons, it is doubtful that the graphene layers are flat [12]. Nevertheless, due to the importance of sodium ions storage, applying an accurate averaged determination method like the Ruland and Smarsly algorithm for WAXS data is highly encouraged.

The stacking parameters L_c and N showed an increasing trend in the current study with the rapid change between materials pyrolysed at 1000 and 1100 °C. These parameters are often reported in battery-related articles and are usually calculated with the Scherrer equation from XRD data [3,20,52,84]. While the collected WAXS patterns of HCs might appear similar, alternative analysis methods can yield significantly different outcomes from the data. For example, Li et al. (2021) [21] reported an L_c value of 3.571 nm for hard carbon synthesised at 1400 °C, but for the current study, all L_c values stayed under 1 nm. Another parameter, interlayer spacing value a_3, considered essential in terms of the intercalation of sodium ions, is attracting considerable critical attention. It has been observed that lower synthesis temperatures of carbons result in higher a_3 values (>0.36 nm) that are more suitable for sodium ion intercalation [7]. However, as a negative side, insufficient T_p can result in an ultra-microporous structure alongside an overlarge specific surface area, leading to a decreased coulombic efficiency on the first cycle of the battery due to extensive electrolyte decomposition on the material's surface.

A study by Chen et al. (2021) [13] suggests that the low-potential sloping region in the charge (-discharge) curve is associated with the sodium ion intercalation between the turbostratic graphene layers. Increasingly, attempts have been made to correlate electrochemically measured parameters such as established first discharge/charge capacity values or capacity values at different states of charge with the HC interlayer spacing value a_3 [4,6,7,9,10,21]. So far, interlayer spacing parameters have been calculated from XRD data applying the Bragg equation, establishing the a_3 value reaching up to 0.420 nm [9]. Data from several publications have identified that the optimal interlayer spacing needed to be $a_3 > 0.37$ nm by Li et al. 2021 [21], $a_3 = 0.38$ nm by Matei Ghimbeu et al. (2018) [10] and $a_3 = 0.39$ nm by Kumaresan

et al. (2021) [20]. According to the density-functional theory calculations by Cao et al. (2012) [85], the threshold of interlayer spacing needed for storing sodium ions is approximately 0.37 nm. Hence, the estimation of this parameter *ex situ* in time and space and its subsequent correlation with electrochemical measurements certainly poses the question of whether the initial interlayer spacing of HC is vital for optimal SIBs.

Understanding the complexity of the sodium ion intercalation mechanism is essential to remember that the interpretation is even more challenging since the interlayer spacing is a dynamic value that changes continuously during the charging and discharging steps [12,49,86]. Nevertheless, according to several reports, T_p affects the interlayer spacing, the a_3 parameter, showing a decreasing trend with increasing pyrolysis temperature [34,48,87,88]. No distinguishable trend was observed for the HCs investigated in this study, and the a_3 value ranged from 0.362 to 0.375 nm for all HCs analysed (Fig. 3).

To determine whether both analysis approaches would yield consistent results, a_3 and L_c parameters for HCs under discussion were calculated with commonly used Bragg and Scherrer equations (Table S4 in SI) and compared with the results from the complete WAXS pattern analysis approach used in this study (Table 2). Fig. 3 compares the experimental data on the interlayer spacing values of HCs reported in SIB-based studies [7,9,10,21,34] and calculated in this study. The findings indicate that the a_3 values computed using the Bragg equation consistently showed higher values than those derived from the comprehensive pattern analysis using the Ruland and Smarsly algorithm. Furthermore, the a_3 values calculated directly from the peak position using the Bragg equation exhibit higher uncertainties. While the calculation of the a_3 value using the Ruland and Smarsly algorithm fundamentally adheres to the Bragg law, it additionally accommodates the inclusion of the polarisation factor and instrumental broadening within the same line profile fitting procedure without the need to separate scattering peaks [30,39]. When comparing with data from the literature, it can be challenging to ascertain whether the initial processing of XRD data considers the inclusion of Lorentz polarisation factors. However, it is known that this assessment is essential for any analysis that depends on the intensity of X-ray diffraction maxima. One of the most notable findings from the data analysis was that the interlayer spacing values for the HCs examined in this study were lower than

those reported in prior publications for HCs subjected to similar pyrolysis temperatures. This discrepancy can be attributed to the omission of the aforementioned Lorentz polarisation factors. Thus, employing the Bragg equation may result in overestimated a_3 values. Consequently, any further refined conclusions drawn for the optimisation of interlayer spacing in SIBs should be approached with caution. The following part of this paper describes in greater detail how the model-free SAS analysis could aid in establishing a better understanding of the disorder of the graphene layer structure, change in porosity and degree of disorder in HCs.

3.3. Structural parameters related to porosity in HCs determined by SANS

SANS analysis described in this chapter examines the effect of the pyrolysis temperature, T_p, on the nanoscopic properties of the HCs at the length scale >0.6 nm (Fig. 4). The SAXS model-free analysis approach introduced by Ruland and coworkers [54–57] (Eqs. S9–S17 in SI) consists of separating the measured macroscopic scattering cross-section per unit mass of carbon, $\frac{d\sum_m}{d\Omega}$, into the scattering from the density fluctuations of the carbon material, $\frac{d\sum_{fluct}}{d\Omega}(q)$ and the scattering originating from the porous structure of the carbon, $\frac{d\sum_{pores}}{d\Omega}(q)$ (Eqs. S10 and S11 in SI) (Fig. 4b). After considering the fluctuation component, $\frac{d\sum_{fluct}}{d\Omega}(q)$, the rise of the pore scattering curve, $\frac{d\sum_{pores}}{d\Omega}(q)$, in the high q region with a slope corresponding to q^{-4}, related to an ideal two-phase porous structure (Fig. 4b; Figs. S6b and S7 in SI).

Observation of the SANS scattering patterns shows that the macroscopic scattering cross-section curves do not respond to the slope of q^{-4} in the high scattering vector q area, which indicates that there are density fluctuations in the carbon phase of the materials under study (Fig. 4a; Fig. S6a in SI) [56]. The tail of the scattering curve for hard carbons produced at pyrolysis temperatures of 700 °C or 1000 °C primarily exhibits a q^{-2} decay, corresponding to the carbon solid phase, namely, the fluctuations in the pore walls. This observation aligns with the methodology pioneered by Ruland, explicitly tailored for porous carbons [54–57]. Nonetheless, as the pyrolysis temperature increases, the q^{-4} slope becomes more pronounced in the high scattering vector q
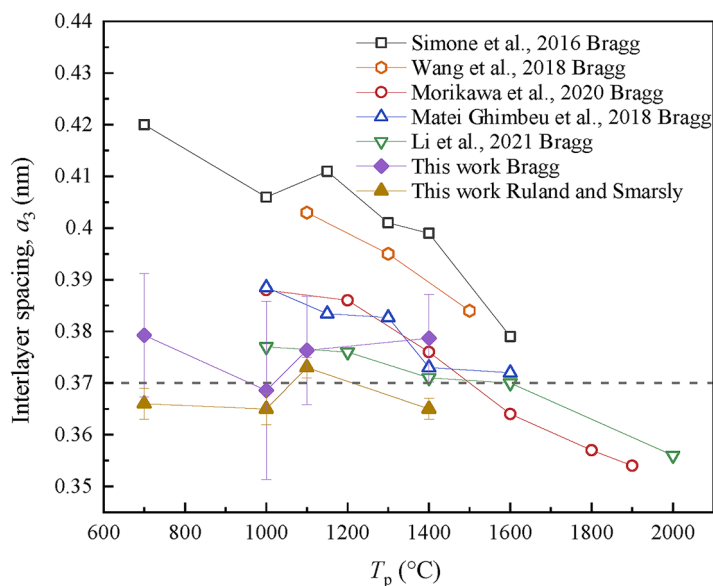

Fig. 3. Comparing the interlayer spacing values of hard carbons derived from various precursors as documented in studies related to SIBs [7,9,10,21,34] (uncertainties not provided) and calculated in this study depending on the synthesis temperature of the hard carbon. Additionally, the calculations were carried out by applying the Bragg equation to control for bias (Table S4 in SI). The dashed line marks the threshold of interlayer spacing needed for storing sodium ions according to the density functional theory calculations by Cao et al. (2012) [85].
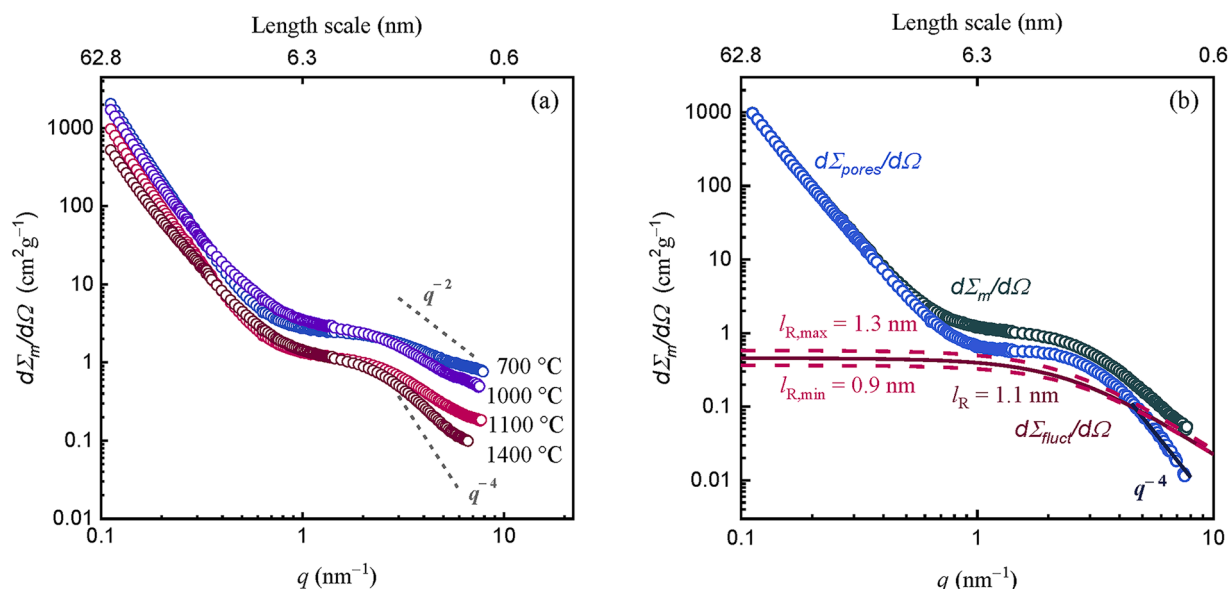
Fig. 4. (a) The macroscopic scattering cross sections, $\frac{d\sum_m}{d\Omega}(q)$ of d-glucose derived carbon materials with different T_p (noted in Figure). (b) Statistically independent components of the differential scattering cross-section of GDC-1100 material. The dashed lines show the fluctuation component's limits for the maximum Ruland length, $l_{R,max}$ and the minimum possible Ruland length, $l_{R,min}$. The boundaries of the fluctuation component are established to ensure that it remains within the range of the macroscopic scattering cross-section, and the slope in the high q region aligns with a decay proportional to q^{-4}, signifying the scattering from the two-phase structure of pores and pore walls. The setting of l_R comes with an associated uncertainty of approximately 10 %. (For other HCs, see Figs. S6 and S7 in SI).

region. Therefore, it is reasonable to postulate that the high q-range decay comprises both a q^{-2} and a q^{-4} component, where the q^{-4} component pertains to the scattering arising from the two-phase structure of pores and now the homogeneous pore walls (Fig. S7 in SI). In conjunction with assessing and incorporating the fluctuation component, the analysis yields 13 structural parameters for the sake of integrity, detailed in Table 3.

The parameters such as background C, the fluctuation component B_{fl}, Porod constant P_m, inner surface S/m and Ruland length l_R outlined in Table 3 are computed and established by plotting the measured scattering curve without applying any model. The following parameters in Table 3 are derived after considering the impact of fluctuation (Fig. S8 in SI). Readers are referred to references [54,89] for a more in-depth understanding of this model-free analysis method.

The next chapter displays the combination of WAXS and SANS structural parameters to explain the differences in the sloping and plateau capacity proportion in the second cycle of the sodiation curves. The focus is on assessing the parameters with significant potential for influencing electrochemical performance.

3.4. Empirical correlation between the structure of hard carbon and specific capacity

It was previously demonstrated that there are apparent differences between the specific capacity values for GDC-1000 and GDC-1100, which cannot be explained by the gas physisorption measurement results (chapter 3.1, Fig. S3 in SI). The physical meaning of the l_R parameter is similar to that of L_a obtained from the WAXS analysis. The value of both parameters describes the lateral length of the layer and shows an increase as the pyrolysis temperature increases T_p (Tables 2 and 3; Fig. 5a; Fig. S7 in SI). However, since the l_R parameter also carries information about the curvature of the graphene-like layer, the L_a parameter's value may diverge from that of l_R. Thus, the difference in l_R and L_a should be more prominent if the layers contain more defects and higher curvature. In the case of WAXS analysis, an increase in L_a value indicates an increase in the diameter of the graphene layer. The l_R value obtained from SANS analysis shows the size of the uncurved and defect-free graphene layer. Morikawa et al. (2020) [7] proposed that sodium

adsorption on the graphene layer occurs in the edges and defect sites. Therefore, parallel analysis of L_a and l_R could carry essential information about the ability to adsorb sodium ions on/in the graphene layers.

As shown in Fig. 5b, as the graphene layer curvature exceeds 1 nm and an average graphene layer extent surpasses 6.3 nm, the plateau capacity value stays constant, indicating that the HC is less curved and has a larger defect-free graphene layer area. However, the sloping capacity value falls rather than remains constant for GDC-1400 material, showing the optimum interval needed between the L_a and l_R that favours the sodium ions adsorption on defect sites, i.e., the decline in the sloping capacity value can be related to the interaction of the sodium cations with graphene edges.

Moreover, the empirical relationship between lateral length characteristics and specific capacity sub-regions correlates well with the interlayer spacing change presented in Fig. 3, indicating that as the pyrolysis temperature increases, the hard carbons more and more involved structures with hydrogen-free edges and not only a_3 change plays a role, but also the interval between the static parameters L_a and l_R (Fig. 5b). In light of the provided data in this study, we suggest that the relationship between the diameter of the graphene layer extent, L_a, and the curvature of the graphene layer, l_R, serves as a metric through which the extent of the interlayer surface structure, along with its energetically appropriate curvature repetition across the graphene layer, is influenced by the consistent preservation of a_3 throughout this area. In other words, consider a scenario where the graphene layer extent is relatively short ($L_a = 4.2 \pm 0.7$) with the curvature of $l_R = 0.65 \pm 0.08$ (convex/concave). In such a case, the interconversion probability during the electrochemical charge and discharge process is higher for the mentioned "unit graphene layer cells" compared to graphene layers with a larger extent ($L_a = 7 \pm 1$) with $l_R = 1.1 \pm 0.2$. Moreover, it encompasses a wider range in which a_3 is considered 0.373 ± 0.002 at various spatial locations. The interconnected parallel graphene layers could facilitate compensation for local surface charge between their surfaces, thereby promoting the formation of pseudometallic Na.

Additionally, it has been shown that the armchair edges are more thermodynamically favourable with lower formation energy compared to zigzag edges [90,91]. Therefore, it is expected that the GDC-1400 sample has more H-free armchair edges in comparison to the

Table 3
Small-angle neutron scattering analysis results.

	Parameter	GDC-700	GDC-1000	GDC-1100	GDC-1400	Trend
Parameters calculated from raw data	C (cm²g⁻¹)	0.69 ± 0.04	0.40 ± 0.03	0.13 ± 0.05	0.037 ± 0.006	↓
	B_{fl} (cm²nm⁻² g⁻¹)	7 ± 2	7 ± 2	2.3 ± 0.3	1.8 ± 0.3	↓
	P_m (cm²g⁻¹nm⁻⁴)	0.05 ± 0.03	0.03 ± 0.01	0.026 ± 0.004	0.025 ± 0.003	–
	S/m (m² g⁻¹)	419 ± 237	382 ± 157	257 ± 32	170 ± 20	↓
	l_R (nm)	0.65 ± 0.08	0.9 ± 0.1	1.1 ± 0.2	1.4 ± 0.2	↑
Porosity related parameters	Q_m (cm²g⁻¹nm⁻³)	1.8 ± 0.6	1.7 ± 0.5	1.0 ± 0.2	0.8 ± 0.2	↓
	ϕ	0.8 ± 0.3	0.8 ± 0.2	0.5 ± 0.1	0.3 ± 0.1	↓
	l_p (nm)	0.6 ± 0.4	0.6 ± 0.3	0.5 ± 0.1	0.6 ± 0.2	–
	l_{pores} (nm)	3.2 ± 2.2	2.8 ± 1.4	1.0 ± 0.2	0.9 ± 0.2	↓
	l_{solid} (nm)	0.7 ± 0.5	0.8 ± 0.4	1.2 ± 0.3	1.8 ± 0.5	↑
	l_c (nm)	7.6 ± 2.5	7.1 ± 2.0	6.5 ± 1.5	5.5 ± 1.4	↓
	l_c/l_p	12.7 ± 2.5	11.3 ± 2.0	11.9 ± 1.5	8.8 ± 1.4	↓
	$\frac{\Delta^2 a_3'}{a_3^2} + \frac{\Delta^2 l_R}{l_R^2}$	1.5 ± 0.6	1.4 ± 0.4	0.49 ± 0.07	0.38 ± 0.07	↓
	$\frac{\Delta^2 a_3}{a_3^2} + \frac{\Delta^2 l_R}{l_R^2}$	1.4 ± 0.5	1.3 ± 0.4	0.44 ± 0.07	0.35 ± 0.06	↓

C – background scattering (↓); B_{fl} – fluctuation component (↓); P_m – Porod constant; S/m – inner surface (↓); l_R – lateral correlation length, e.g. Ruland length (↑); Q_m – invariant Q sum (↓); ϕ – porosity (↓); l_p – average chord length, e.g. Porod length; l_{pores} – average chord length of the pore (↓); l_{solid} – average chord length of pore walls (↑); l_c – length of coherence (↓); l_c/l_p – anisometric ratio, describing the shape of the pores (↓); $\frac{\Delta^2 a_3'}{a_3^2} + \frac{\Delta^2 l_R}{l_R^2}$ – degree of disorder, calculated from fixed interlayer spacing a_3' (↓), $\frac{\Delta^2 a_3}{a_3^2} + \frac{\Delta^2 l_R}{l_R^2}$ – degree of disorder, calculated from interlayer spacing a_3, derived from WAXS analysis (↓). The error values denote the standard deviation of the measurement; the error for the Ruland length parameter is an absolute error estimated via the limits of the fluctuation component.

GDC-1100. However, H-free edges involve carbon dangling bonds, which more strongly interact with sodium cations. Our quantum-chemical calculations show that the interaction energy between the sodium ions and H-free graphene edges can be an order of magnitude stronger than that between sodium cations and graphene sheets with fully hydrogenated edges (−1.54 eV vs. −0.18 eV), which are more likely to form in the samples synthesised at lower temperatures. This strong interaction could hinder the intercalation process, which, in turn, could result in lower sloping capacity values.

3.5. Role of the open and closed porosity of hard carbons

The Kratky plot is constructed to describe the microporosity of HC materials in more detail, showing the dependence of the scattered signal intensity from the pores and the scattering vector q (Fig. 6a). The Kratky plot's $\frac{d\sum_{pores}}{d\Omega}(q)q^2$ vs q area under the curve expresses the material's microporosity per mass (i.e., characterising open and closed pores). It is observed that the integral over $\frac{d\sum_{pores}}{d\Omega}(q)q^2$, decreases with an increasing

T_p. The highest ϕ value is established for the material pyrolysed at 700 °C, and the lowest ϕ is calculated for the material pyrolysed at 1400 °C (Table 3). The resulting difference in GDC-1000 and GDC-1100 overall porosity (i.e. including open and closed pores) derived from SANS analysis is outstanding, yet the difference between the open pore volume of the HCs established by gas physisorption analysis is not evident (Fig. 6a and Fig. S3 in SI). This finding indicates the varying differences between the accessible open pore volume and the closed pore volume formation in HCs under study.

The most prominent change with pyrolysis temperature is a reversed "z-shaped" shift of the position of the peak to the direction of lower q-values, which implies a two-way change in the hierarchical structure of the HC and overall porosity. The shift towards the lower q-values (GDC-700 vs GDC-1000) seems to be caused by the arrangement of the graphene layers, yet not by the formation of the stacks (the reader is referred to WAXS analysis, L_a, in chapter 3.2) as the overall porosity at the nanoscopic level remains constant (Table 3). However, the rapid decrease of the integral over $\frac{d\sum_{pores}}{d\Omega}(q)q^2$, (GDC-1000 vs. GDC-1100) indicates the three-dimensional ordering of the turbostratic layers and the growth of the stacks in GDC-1100 (L_a and L_c in Table 2). It also follows that using a synthesis temperature only 100° higher than before (1000 °C and 1100 °C) promotes the formation of transport pores of the same size as the pore wall thickness. The most appropriate parameter compatibility is achieved for the GDC-1100 material, where L_c, l_{pore} and l_{solid} values are of the same order of magnitude (Fig. 6b, Tables 2 and 3), being important from SIBs development perspective.

The analysis suggests that the hierarchical change in the structure of HCs induced by pyrolysis temperature is subsequential at two different length scales, i.e., changes in porous structure in length scale from 1.8 to 2.3 nm (nanoscopic scale) are correlated to the layered structure described in length scale from 0.34 to 0.39 nm (atomic scale). The highest pyrolysis temperature (T_p = 1400 °C) applied results in a pore wall twice as thick as the pore size and the shift towards the lower q-values (GDC-1100 vs. GDC-1400), indicating no further loss of the overall porosity. With the increased material regularity, HC's layers become broader, and the previously existing voids grow together, increasing the uniformity of the carbon material. The higher anisometric ratio of 12.7 indicates a broad distribution of chord length due to an asymmetric shape of the pores and decreases with a further rise of T_p (Table 3). The anisometric ratio value shows that the pores get less asymmetric at higher T_p, contributing to sodium ion storage, as the specific plateau capacity value is further increased for the GDC-1400 material. Additionally, to highlight that the HC's internal curvature and the area's width, i.e., the interval between the L_a and l_R, has extended further with the increase of T_p up to 1400 °C.

To further evaluate the impact of the closed porosity of the HCs under study, two approaches were used (Fig. 6b). The first approach used by Li et al. (2019) [92] allows to calculate closed pore volume from the density of the hard carbon (Eq. S18 in SI). The densities of the HCs were calculated by combining the approach introduced by Saurel et al. [49] (Eqs. S19, S20 and Table S5 in SI) and applying the porosity values estimated via SANS analysis in this work (Table 3). The second approach introduced by Xiao et al. [93] allows the calculation of closed pore volume from the specific plateau capacity values (Eq. S21 in SI). The results show that the closed pore volume increases when 1000 °C or 1100 °C have been applied. The finding is controversial to the results when the Li et al. approach is used for calculations, which demonstrated the rapid decrease of the closed pore volume as the pyrolysis temperature increases (Fig. 6b). Thus, there is an excellent correlation between the electrochemical measurements displaying the drastic increase in specific capacity value between materials GDC-1000 and GDC-1100 (Fig. 1b) and the Kratky plot analysis demonstrating the hierarchical changes occurring in the porous structure that promotes the formation of pores of same size as the pore wall thickness at the pyrolysis temperature 1100 °C. This notion shows the closed pores' vital role and the
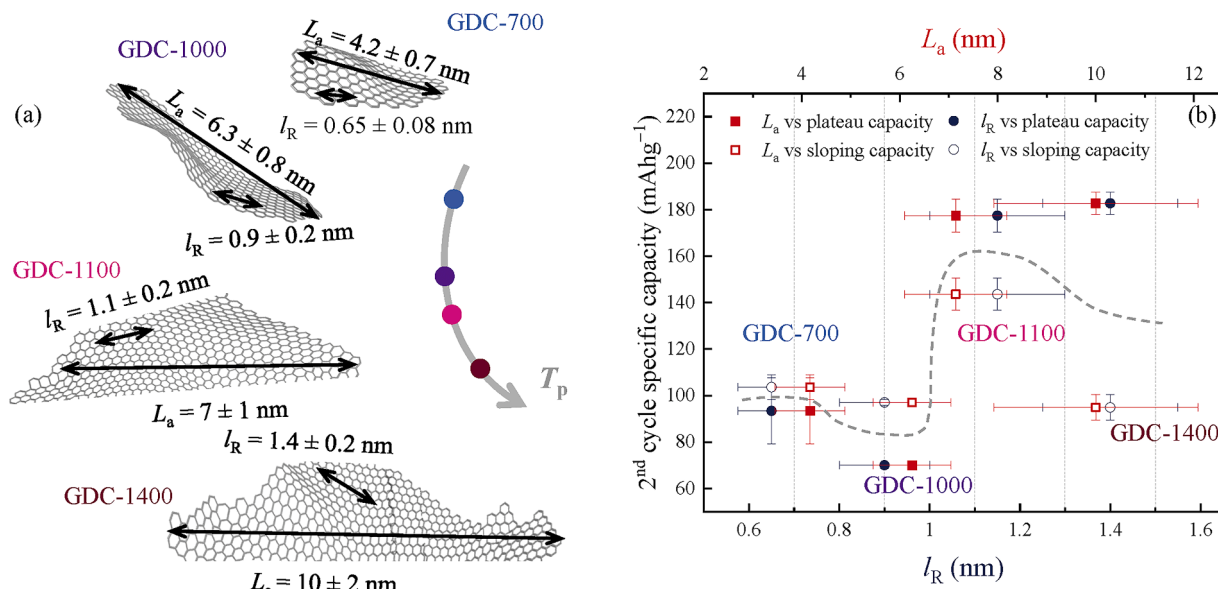
Fig. 5. (a) The diagram illustrating the alterations in the graphene layer in the studied HCs as a function of the T_p according to the obtained L_a and l_R parameters. (b) Empirical correlations between the L_a and l_R parameters and the second cycle sodiation plateau- and sloping specific capacities.
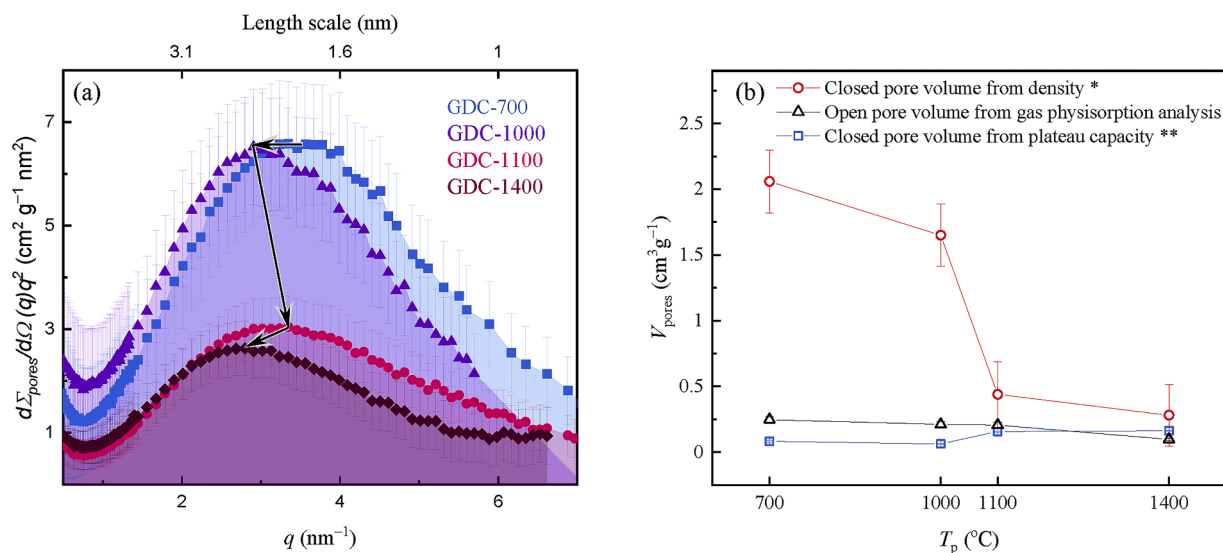

Fig. 6. (a) Kratky plot of hard carbons synthesised from d-glucose by hydrothermal carbonisation at different pyrolysis temperatures (indicated in Figure). The arrows in the Figure indicate the hierarchical changes in the carbon material. This plot reveals rapid overall open- and closed porosity changes between 1000 °C and 1100 °C pyrolysed HCs. These materials also showed changes in the WAXS pattern (002) reflex, where the reflex position difference denotes the changes in the interlayer arrangement. (b) The impact of the pyrolysis temperature of the hard carbon material synthesised from d-glucose on the pore volume from gas physisorption and closed pore volumes calculated using two different approaches. * Li et al. (2019) [92] approach enable the calculation of closed pore volume using XRD peak positions and SANS pore volume fraction (Eqs. S18-S20 in SI). ** Biwei Xiao et al. (2019) [93] approach enables the derivation of closed pore value from plateau capacity (Eq. S21 in SI). Both closed pore volume calculation methods show a discrepancy from open pore volume.

plateau region's length. This structural change cannot be explained by the accessible porosity and pore size distribution analysis via gas physisorption data (chapters 5.1 and 5.2 in SI). The focus of the following discussion is on specific plateau capacity value, which has been reported to be related to the porous structure of the HCs [3,7,10], showcasing the power of the detailed analysis of the porous structure with SANS model-free analysis.

3.6. Interlayer spacing of hard carbons and specific capacity

The intercalation of sodium ions between the graphene layers has been associated with the formation of the plateau region [7,41] in Fig. 1

and Fig.S2 in SI. The interlayer spacing of GDC-1100 0.373 ± 0.002 nm seems sufficient for sodium ions to intercalate between the carbon layers as well as for the accessibility of the pores.

A precise value of the a_3 parameter, obtained in Chapter 3.2, enables us to use it in further SAS analysis to estimate the degree of disorder in the materials under study. The following two approaches were used to identify the degree of disorder: the fixed a_3 value from the literature, graphite interlayer spacing 0.335 nm [56,79] and a_3 value derived from WAXS analysis with Ruland and Smarsly algorithm [44] (Eq. S17 in SI). Comparing the degree of disorder calculated from fixed interlayer spacing a_3 with the degree of disorder calculated from the value of a_3 obtained from the WAXS data analysis is tabulated in Table 3 and

plotted in Fig. 7(a). The pyrolysis temperature affects the degree of disorder obtained using the fixed a_3 and the a_3 value obtained from the WAXS analysis. The higher the T_p, the lower the degree of material disorder, i.e., the material's structure becomes more ordered. The values obtained for the degree of disorder using different a_3 are very similar. This study presented in this report is one of the first investigations to include parameter obtained from the WAXS analysis and employ it in the SANS analysis of hard carbons. The resulting empirical analysis suggests that such a transfer of parameters is justified (Fig. 7a).

The degree of disorder (Eq. S17 in SI) of the porous structure of the material can be compared with the polydispersity of stack height, κ_c, from the WAXS analysis (Eqs. S7 and S8 in SI). Of interest here are the coinciding results at the three highest pyrolysis temperatures, which could be observed because, at lower temperatures, the irregularity of the HC is also higher within the layer, which will play a more important role in considering the total disorder. Fig. 7(a) illustrates the coinciding results of the disorder of the material observed in different methods.

The HCs synthesised at lower temperatures are more disordered, with the change occurring between the materials GDC-1000 and GDC-1100 (Fig. 7a). Three-dimensional ordering arose, resulting in the changes in layered structures and porous structures between these materials. The ordering was also visible when comparing the proportion of the specific sloping- and plateau capacity values from the overall second cycle sodiation curve (Fig. 7b). Hard carbons prepared at lower temperatures have a more dominant sloping capacity value with the noticeable change occurring at 1100 °C. Meaning that HCs synthesised at lower temperatures have smaller, curved and more defective layers, where the sodium ions can adsorb during sodiation and contributing to sloping capacity region, which has also been highlighted in the literature [7,9,41]. For the GDC-700, the polydispersity of stack height is the highest; however, the change in specific capacity values between the GDC-700 and GDC-1000 is not significant. Therefore, it can be concluded that the stack height differences in the material do not contribute to sodium adsorption, and the lateral disorder plays a key role.

We emphasise that the *ex situ* physical characterisation gives an idealised material picture rather than a realistic one. Electrochemical measurements demonstrate an operational system with a considerable role in other phases and processes that might influence the result. The complex layer-by-layer contrast matching procedures would shed light on the processes in real-time to gain a more realistic picture of the sodium storage mechanism. Contrast matching of the hard carbon powders

with deuterated toluene does not give an accurate picture (presented in Fig. S9 in SI), as additional active and binding agents are added during the electrode preparation, significantly altering the pore availability. In addition, the deuterated solvent used for contrast matching differs considerably in its properties from the solvent used in the electrolyte solution. Therefore, this part of the analysis becomes essential when an operando experiment is performed, and then a layer-by-layer approach to contrast match is required.

Taking everything into account, scattering methods combined with electrochemical data analysis provide information about the porous structure of the bulk HC material in detail [81], and thus, it is encouraged to use this methodology for SIB anode research.

4. Conclusions

This study has demonstrated the significant advantages of using wide-angle X-ray (WAXS) and small-angle neutron (SANS) scattering methods to reveal a detailed description of turbostratic d-glucose-derived hard carbons (GDCs). Moreover, it addresses why hard carbon (HC) from the same source but pyrolysed at 1100 °C appears to have better performance properties in SIBs than others pyrolysed at either 700 °C, 1000 °C or 1400 °C. Simultaneously, a set of 12 WAXS and 13 SANS quantified structural parameters were determined and discussed.

This investigation includes interlayer spacing a_3 obtained from the WAXS analysis and employs it in the SANS analysis of HCs. The resulting analysis suggests that such a transfer of parameters is justified and emphasises the importance of applying the accurate Ruland and Smarsly algorithm rather than the widely used Scherrer and Bragg equations. The most prominent finding to emerge from this study is that the Ruland and Smarsly algorithm used in this work systematically yielded a lower value of a_3 compared to the commonly used Bragg equation. Contrary to expectations and previous research data, this study did not find a significant influence of the pyrolysis temperature on the interlayer spacing a_3 parameter [33,46,79,80], and the a_3 value ranged from 0.365 to 0.373 nm for all HCs analysed. The results of this investigation indicate that the interlayer spacing of 0.373 nm means the best fit of the GDC-1100 for sodium-ion battery anode material [77].

The comparison of calculated parameters for HCs prepared at different pyrolysis temperatures showed that the most appropriate parameter compatibility is achieved for the GDC-1100 material, where the values of the average stack height, L_c, the average chord length of the pore, l_{pore} and pore walls, l_{solid} are of the same order of magnitude, i.e.
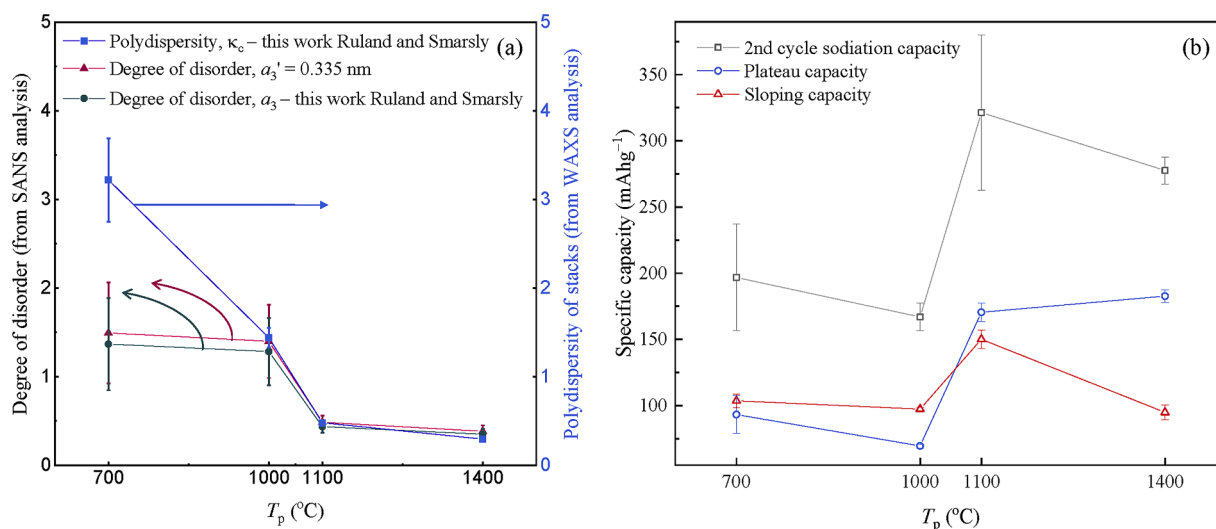

Fig. 7. (a) An empirical comparison of polydispersity of stacks κ_c and degree of disorder parameters: degree of disorder calculated using a_3' or a_3 derived from WAXS analysis (Table 2); (b) The pyrolysis temperature of hard carbon impact on overall-, plateau- and sloping capacity. Hard carbons prepared at lower temperatures have a more dominant sloping capacity, which is affected by a higher degree of disorder and polydispersity of material.

the average pore size and thickness of the pore wall have coinciding quantities, resulting with highest specific capacity value, where the contribution of the capacity component of the plateau predominates. The sudden change in the L_c values was most striking as the temperature increased from 1000 to 1100 °C. No previous study has given sufficient consideration to the interplay between the curvature and defects occurring in the highly turbostratic layers, thus, whether the graphene layer extent, L_a, and the Ruland length, l_R operate simultaneously. Therefore, the parallel analysis of the graphene layer extent, L_a and l_R carries essential information about the ability to adsorb sodium ions on/ in the graphene layers and can be empirically correlated with the specific plateau capacity and sloping capacity values. Thus, the interval between L_a and l_R is of decisive importance here. These deformations have been shown to be necessary for sodium ion adsorption on the graphene layers [7]. Hence, with increased material regularity, HC's layers become broader, and the previously existing voids grow together, increasing the uniformity of hard carbon to promote better sodium ion storage. It can be concluded that the stack height differences in the material do not contribute to the sodium adsorption, but the lateral disorder plays an essential role as the change in specific capacity values between the GDC-700 and GDC-1000 is not significant.

The model-free analysis suggests that the hierarchical change in the structure of HCs induced by pyrolysis is subsequential at two different length scales, i.e., changes in porous structure in length scale from 1.8 to 2.3 nm (nanoscopic scale - SANS) are correlated to the layered structure described in length scale from 0.34 to 0.39 nm (atomic scale – analysed by WAXS method). The results of this investigation emphasise that while a_3 is a dynamic quantity, it seems to have a more significant influence during the sloping region formation stage. The interplay between the a_3 and the interval of the static L_a and l_R parameters favours the further higher contribution of the plateau capacity region. The disparity between these three parameters favours the formation of suitably sized closed pores and, hence, the sodium ion storage stage, i.e. anisometric ratio promoting the sodium ion storage, showing higher specific plateau capacity values. The study demonstrated how to apply a combination of the lateral length parameters to analyse the electrochemical sloping and plateau capacity values. The results correlated empirically with the HCs' electrochemical performance, proving the WAXS/SANS toolbox's suitability for future SIB research.

CRediT authorship contribution statement

Laura Kalder: Writing – original draft, Visualization, Investigation, Data curation. **Annabel Olgo:** Visualization, Investigation, Data curation. **Jonas Lührs:** Software, Investigation, Data curation. **Tavo Romann:** Software. **Riinu Härmas:** Writing – review & editing, Conceptualization. **Jaan Aruväli:** Software, Methodology, Data curation. **Pouya Partovi-Azar:** Supervision, Resources. **Albrecht Petzold:** Software, Methodology. **Enn Lust:** Supervision, Resources, Funding acquisition. **Eneli Härk:** Writing – review & editing, Supervision, Resources, Conceptualization.

Declaration of competing interest

The authors declare that they have no known competing financial interests or personal relationships that could have appeared to influence the work reported in this paper.

Acknowledgements

Supplementary materials

Supplementary material associated with this article can be found, in the online version, at doi:10.1016/j.ensm.2024.103272.

References

[1] S. Alvin, D. Yoon, C. Chandra, R.F. Susanti, W. Chang, C. Ryu, J. Kim, J. Power Sources 430 (2019) 157–168.
[2] M. Arnaiz, J.L. Gómez-Cámer, E. Gonzalo, N.E. Drewett, J. Ajuria, E. Goikolea, M. Galceran, T. Rojo, Mater. Today Proc. 39 (2021) 1118–1131.
[3] D. Cheng, X. Zhou, H. Hu, Z. Li, J. Chen, L. Miao, X. Ye, H. Zhang, Carbon N Y 182 (2021) 758–769.
[4] R. Dong, L. Zheng, Y. Bai, Q. Ni, Y. Li, F. Wu, H. Ren, C. Wu, Adv. Mater. 33 (2021) 2008810.
[5] D. Ledwoch, L. Komsiyska, E.-M. Hammer, K. Smith, P.R. Shearing, D.J.L. Brett, E. Kendrick, Electrochim. Acta 401 (2022) 139481.
[6] Q. Meng, Y. Lu, F. Ding, Q. Zhang, L. Chen, Y.-S. Hu, ACS Energy Lett. 4 (2019) 2608–2612.
[7] Y. Morikawa, S. Nishimura, R. Hashimoto, M. Ohnuma, A. Yamada, Adv. Energy Mater. 10 (2020) 1903176.
[8] A. Rudola, A.J.R. Rennie, R. Heap, S. Shayan Meysami, A. Lowbridge, F. Mazzali, R. Sayers, C.J. Wright, J. Barker, J. Mater. Chem. A 9 (2021) 8279–8302.
[9] V. Simone, A. Boulineau, A. de Geyer, D. Rouchon, L. Simonin, S. Martinet, J. Energy Chem. 25 (2016) 761–768.
[10] C. Matei Ghimbeu, J. Górka, V. Simone, L. Simonin, S. Martinet, C. Vix-Guterl, Nano Energy 44 (2018) 327–335.
[11] N. Sun, Z. Guan, Y. Liu, Y. Cao, Q. Zhu, H. Liu, Z. Wang, P. Zhang, B. Xu, Adv. Energy Mater. 9 (2019) 1901351.
[12] J.K. Mathiesen, R. Väli, M. Härmas, E. Lust, J.F.V. Bulow, K.M.Ø. Jensen, P. Norby, J. Mater. Chem. A 7 (2019) 11709–11717.
[13] X. Chen, Y. Fang, H. Lu, H. Li, X. Feng, W. Chen, X. Ai, H. Yang, Y. Cao, Small 17 (2021) 2102248.
[14] S. Alvin, C. Chandra, J. Kim, Chem. Eng. J. 411 (2021) 128490.
[15] M. Zhang, Y. Li, F. Wu, Y. Bai, C. Wu, Nano Energy 82 (2021) 105738.
[16] L.-F. Zhao, Z. Hu, W.-H. Lai, Y. Tao, J. Peng, Z.-C. Miao, Y.-X. Wang, S.-L. Chou, H.-K. Liu, S.-X. Dou, Adv. Energy Mater. 11 (2021) 2002704.
[17] D. Alvira, D. Antorán, J.J. Manyà, Chem. Eng. J. 447 (2022) 137468.
[18] K. Schutjajew, P. Giusto, E. Härk, M. Oschatz, Carbon N Y 185 (2021) 697–708.
[19] I.K. Ilic, K. Schutjajew, W. Zhang, M. Oschatz, Carbon N Y 186 (2022) 55–63.
[20] T.K. Kumaresan, S.A. Masilamani, K. Raman, S.Zh. Karazhanov, R. Subashchandrabose, Electrochim. Acta 368 (2021) 137574.
[21] R.-R. Li, X.-X. He, Z. Yang, X.-H. Liu, Y. Qiao, L. Xu, L. Li, S.-L. Chou, Mater. Chem. Front. 5 (2021) 7595–7605.
[22] A. Gomez-Martin, J. Martinez-Fernandez, M. Ruttert, M. Winter, T. Placke, J. Ramirez-Rico, Chem. Mater. 31 (2019) 7288–7299.
[23] D.B. Schuepfer, F. Badaczewski, J.M. Guerra-Castro, D.M. Hofmann, C. Heiliger, B. Smarsly, P.J. Klar, Carbon N Y 161 (2020) 359–372.
[24] B. Yang, J. Wang, Y. Zhu, K. Ji, C. Wang, D. Ruan, Y. Xia, J. Power Sources 492 (2021) 229656.
[25] M.S. Amer, P. O'Brien, H. Craighead, Raman Spectrosc. Fuller. Nanotechnol. R. Soc. Chem. (2010) 43–101.
[26] A. Cuesta, P. Dhamelincourt, J. Laureyns, A. Martínez-Alonso, J.M.D. Tascón, Carbon N Y 32 (1994) 1523–1532.
[27] C. Hu, S. Sedghi, A. Silvestre-Albero, G.G. Andersson, A. Sharma, P. Pendleton, F. Rodríguez-Reinoso, K. Kaneko, M.J. Biggs, Carbon N Y 85 (2015) 147–158.
[28] M. Thommes, K. Kaneko, A.V. Neimark, J.P. Olivier, F. Rodriguez-Reinoso, J. Rouquerol, K.S.W. Sing, Pure Appl. Chem. 87 (2015) 1051–1069.
[29] X. Li, X. Sun, X. Hu, F. Fan, S. Cai, C. Zheng, G.D. Stucky, Nano Energy 77 (2020) 105143.
[30] X. Dou, I. Hasa, D. Saurel, C. Vaalma, L. Wu, D. Buchholz, D. Bresser, S. Komaba, S. Passerini, Mater. Today 23 (2019) 87–104.
[31] D. Chen, W. Zhang, K. Luo, Y. Song, Y. Zhong, Y. Liu, G. Wang, B. Zhong, Z. Wu, X. Guo, Energy Environ. Sci. 14 (2021) 2244–2262.
[32] Y. Matsukawa, F. Linsenmann, M.A. Plass, G. Hasegawa, K. Hayashi, T.-P. Fellinger, Beilstein J. Nanotechnol. 11 (2020) 1217–1229.
[33] A.A. Arie, H. Kristianto, E. Demir, R.D. Cakan, Mater. Chem. Phys. 217 (2018) 254–261.
[34] Q. Wang, X. Zhu, Y. Liu, Y. Fang, X. Zhou, J. Bao, Carbon N Y 127 (2018) 658–666.
[35] A.L. Patterson, Phys. Rev. 56 (1939) 978–982.
[36] P. Scherrer, Nachrichten von der Gesellschaft der Wissenschaften zu Göttingen, Math.-Phys. Kl. 1918 (1918) 98–100.
[37] J.M. Stratford, A.K. Kleppe, D.S. Keeble, P.A. Chater, S.S. Meysami, C.J. Wright, J. Barker, M.-M. Titirici, P.K. Allan, C.P. Grey, J. Am. Chem. Soc. 143 (2021) 14274–14286.
[38] O. Osswald, M.O. Loeh, F.M. Badaczewski, T. Pfaff, H.E. Fischer, A. Franz, J.-U. Hoffmann, M. Reehuis, P.J. Klar, B.M. Smarsly, C 9 (2023) 27.

[39] R. Väli, J. Aruväli, M. Härmas, A. Jänes, E. Lust, Batteries 5 (2019) 56.
[40] H. Au, H. Alptekin, A.C.S. Jensen, E. Olsson, C.A. O'Keefe, T. Smith, M. Crespo-Ribadeneyra, T.F. Headen, C.P. Grey, Q. Cai, A.J. Drew, M.-M. Titirici, Energy Environ. Sci. 13 (2020) 3469–3479.
[41] S. Alvin, D. Yoon, C. Chandra, H.S. Cahyadi, J.-H. Park, W. Chang, K.Y. Chung, J. Kim, Carbon N Y 145 (2019) 67–81.
[42] R. Väli, A. Jänes, T. Thomberg, E. Lust, Electrochim. Acta 253 (2017) 536–544.
[43] R. Väli, A. Jänes, T. Thomberg, E. Lust, J. Electrochem. Soc. 163 (2016) A1619–A1626.
[44] W. Ruland, B. Smarsly, J. Appl. Crystallogr. 35 (2002) 624–633.
[45] T. Pfaff, F.M. Badaczewski, M.O. Loeh, A. Franz, J.-U. Hoffmann, M. Reehuis, W. G. Zeier, B.M. Smarsly, J. Phys. Chem. C 123 (2019) 20532–20546.
[46] F.M. Badaczewski, M.O. Loeh, T. Pfaff, D. Wallacher, D. Clemens, B.M. Smarsly, Beilstein J. Nanotechnol. 11 (2020) 310–322.
[47] K. Faber, F. Badaczewski, M. Oschatz, G. Mondin, W. Nickel, S. Kaskel, B. M. Smarsly, J. Phys. Chem. C 118 (2014) 15705–15715.
[48] K. Faber, F. Badaczewski, W. Ruland, B.M. Smarsly, Z. Für Anorg. Allg. Chem. 640 (2014) 3107–3117.
[49] D. Saurel, J. Segalini, M. Jauregui, A. Pendashteh, B. Daffos, P. Simon, M. Casas-Cabanas, Energy Storage Mater. 21 (2019) 162–173.
[50] D. Saurel, J. Ségalini, M. Jáuregui, A. Pendashteh, B. Daffos, P. Simon, M. Casas-Cabanas, Energy Storage Mater. 28 (2020) 418.
[51] D.A. Stevens, J.R. Dahn, J. Electrochem. Soc. 147 (2000) 4428–4431.
[52] B. Tratnik, N. Van de Velde, I. Jerman, G. Kapun, E. Tchernychova, M. Tomšič, A. Jamnik, B. Genorio, A. Vizintin, R. Dominko, ACS Appl. Energy Mater. (2022).
[53] R. Palm, R. Härmas, E. Härk, B. Kent, H. Kurig, M. Koppel, M. Russina, I. Tallo, T. Romann, J. Mata, K. Tuul, E. Lust, Carbon N Y 171 (2021) 695–703.
[54] E. Härk, M. Ballauff, C 6 (2020) 82.
[55] W. Ruland, J. Appl. Crystallogr. 4 (1971) 70–73.
[56] C. Schiller, J. Mering, P. Cornuault, F.Du Chaffaut, Carbon N Y 5 (1967) 507–516.
[57] R. Perret, W. Ruland, J. Appl. Crystallogr. 1 (1968) 308–313.
[58] M. Teusner, J. Mata, N. Sharma, Curr. Opin. Electrochem. 34 (2022) 100990.
[59] Y.B. Melnichenko, G.D. Wignall, J. Appl. Phys. 102 (2007) 021101.
[60] J. Zhang, G. Cheng, Energy Fuels 35 (2021) 1957–1965.
[61] J. Méring, D. Tchoubar, J. Appl. Crystallogr. 1 (1968) 153–165.
[62] M. Härmas, T. Thomberg, A. Jänes, J. Electrochem. Soc. 167 (2020) 080533.
[63] F. Sun, H. Wang, Z. Qu, K. Wang, L. Wang, J. Gao, J. Gao, S. Liu, Y. Lu, Adv. Energy Mater. 11 (2021) 2002981.
[64] X. Feng, Y. Bai, M. Liu, Y. Li, H. Yang, X. Wang, C. Wu, Energy Environ. Sci. 14 (2021) 2036–2089.
[65] U. Keiderling, Appl. Phys. A 74 (2002) s1455–s1457.
[66] T.D. Kühne, M. Iannuzzi, M. Del Ben, V.V. Rybkin, P. Seewald, F. Stein, T. Laino, R. Z. Khaliullin, O. Schütt, F. Schiffmann, D. Golze, J. Wilhelm, S. Chulkov, M. H. Bani-Hashemian, V. Weber, U. Borštnik, M. Taillefumier, A.S. Jakobovits, A. Lazzaro, H. Pabst, T. Müller, R. Schade, M. Guidon, S. Andermatt, N. Holmberg, G.K. Schenter, A. Hehn, A. Bussy, F. Belleflamme, G. Tabacchi, A. Glöß, M. Lass,
I. Bethune, C.J. Mundy, C. Plessl, M. Watkins, J. VandeVondele, M. Krack, J. Hutter, J. Chem. Phys. 152 (2020) 194103.
[67] J. VandeVondele, J. Hutter, J. Chem. Phys. 127 (2007) 114105.
[68] S. Goedecker, M. Teter, J. Hutter, Phys. Rev. B 54 (1996) 1703–1710.
[69] A.D. Becke, Phys. Rev. A 38 (1988) 3098–3100.
[70] C. Lee, W. Yang, R.G. Parr, Phys. Rev. B 37 (1988) 785–789.
[71] S. Grimme, J. Antony, S. Ehrlich, H. Krieg, J. Chem. Phys. 132 (2010) 154104.
[72] S.F. Boys, F. Bernardi, Mol. Phys. 19 (1970) 553–566.
[73] T. Chen, X. Liu, L. Niu, Y. Gong, C. Li, S. Xu, L. Pan, Inorg. Chem. Front. 7 (2020) 567–582.
[74] M.P. Mercer, M. Nagarathinam, E. Maximiliano Gavilán-Arriazu, A. Binjrajka, S. Panda, H. Au, M. Crespo-Ribadeneyra, M.-M. Titirici, E.P.M. Leiva, H.E. Hoster, J. Mater. Chem. A 11 (2023) 6543–6555.
[75] A. Beda, F. Rabuel, M. Morcrette, S. Knopf, P.-L. Taberna, P. Simon, C.M. Ghimbeu, J. Mater. Chem. A 9 (2021) 1743–1758.
[76] A.C. Ferrari, Solid State Commun 143 (2007) 47–57.
[77] R. Härmas, R. Palm, H. Kurig, L. Puusepp, T. Pfaff, T. Romann, J. Aruväli, I. Tallo, T. Thomberg, A. Jänes, E. Lust, C 7 (2021) 29.
[78] J. Ribeiro-Soares, M.E. Oliveros, C. Garin, M.V. David, L.G.P. Martins, C. A. Almeida, E.H. Martins-Ferreira, K. Takai, T. Enoki, R. Magalhães-Paniago, A. Malachias, A. Jorio, B.S. Archanjo, C.A. Achete, L.G. Cançado, Carbon N Y 95 (2015) 646–652.
[79] R.E. Franklin, J.T. Randall, Proc. R. Soc. Lond. Ser. Math. Phys. Sci. 209 (1951) 196–218.
[80] F. Badaczewski, M.O. Loeh, T. Pfaff, S. Dobrotka, D. Wallacher, D. Clemens, J. Metz, B.M. Smarsly, Carbon N Y 141 (2019) 169–181.
[81] J.N. Rouzaud, A. Oberlin, Carbon N Y 27 (1989) 517–529.
[82] M. Thompson, Q. Xia, Z. Hu, X.Song Zhao, Mater. Adv. 2 (2021) 5881–5905.
[83] H. Tonnoir, D. Huo, C. Davoisne, A. Celzard, V. Fierro, D. Saurel, M. El Marssi, M. Benyoussef, P. Meunier, R. Janot, Carbon N Y 208 (2023) 216–226.
[84] J. Li, T. Li, C. Peng, J. Li, H. Zhang, J. Electrochem. Soc. 169 (2022) 070517.
[85] Y. Cao, L. Xiao, M.L. Sushko, W. Wang, B. Schwenzer, J. Xiao, Z. Nie, L.V. Saraf, Z. Yang, J. Liu, Nano Lett. 12 (2012) 3783–3787.
[86] C. Bommier, T.W. Surta, M. Dolgos, X. Ji, Nano Lett. 15 (2015) 5888–5892.
[87] K. Wang, Y. Xu, Y. Li, V. Dravid, J. Wu, Y. Huang, J. Mater. Chem. A 7 (2019) 3327–3335.
[88] F. Wu, M. Zhang, Y. Bai, X. Wang, R. Dong, C. Wu, ACS Appl. Mater. Interfaces 11 (2019) 12554–12561.
[89] E. Härk, A. Petzold, G. Goerigk, S. Risse, I. Tallo, R. Härmas, E. Lust, M. Ballauff, Carbon N Y 146 (2019) 284–292.
[90] S. Okada, Phys. Rev. B 77 (2008) 041408.
[91] Y. Liu, A. Dobrinsky, B.I. Yakobson, Phys. Rev. Lett. 105 (2010) 235502.
[92] Y. Li, Y. Lu, Q. Meng, A.C.S. Jensen, Q. Zhang, Q. Zhang, Y. Tong, Y. Qi, L. Gu, M.-M. Titirici, Y.-S. Hu, Adv. Energy Mater. 9 (2019) 1902852.
[93] B. Xiao, T. Rojo, X. Li, ChemSusChem 12 (2019) 133–144.